Shock Waves (2011) 21:175–191
DOI 10.1007/s00193-011-0312-4

ORIGINAL ARTICLE

Computational and experimental study of supersonic flow over axisymmetric cavities

K. Mohri · R. Hillier

Received: 12 October 2009 / Revised: 26 November 2010 / Accepted: 20 January 2011 / Published online: 10 April 2011

Abstract Laminar and turbulent computations are presented for annular rectangular-section cavities, on a body of revolution, in a Mach 2.2 flow. Unsteady 'open cavity flows' result for all laminar computations for all cavity length-to-depth ratios, L/D (1.33, 10.33, 11.33 and 12.33). The turbulent computations produce 'closed cavity flows' for L/D of 11.33 and 12.33. Surface pressure fluctuations at the front corner of the $L/D = 1.33$ cavity are periodic in some cases depending on the cavity length and depth, the boundary layer at the cavity front lip and the cavity scale. The turbulent computations are supported by experimental schlieren images, obtained using a spark light source, and time-averaged surface pressure data.

Keywords Supersonic cavities · Axisymmetric cavities · Annular cavities · Laminar and turbulent supersonic cavities

Communicated by F. Seiler.

This paper was based on work that was presented at the 26th International Symposium on Shock Waves, Goettingen, Germany, July 15–20, 2007.
K. Mohri was awarded with the ISWI (The International Shock Wave Institute) Student Award for the best student presentation at the Symposium.

K. Mohri · R. Hillier
Department of Aeronautics, Imperial College London, London, UK

Present Address:
K. Mohri (✉)
Institute for Combustion and Gasdynamics,
University of Duisburg-Essen, Essen, Germany
e-mail: khadijeh.mohri@uni-due.de

1 Introduction

This paper presents both computational and experimental results for Mach 2.2 flow over annular cavities, of rectangular section, on a body of revolution as shown in Fig. 1.

Rectangular cavities have been classified into three main flow groups [1,2]. In an *open cavity* the separated shear layer spans the cavity and reattaches onto the rear face at or near the top corner and in a *closed cavity* it reattaches on the cavity floor. The intermediary state between the two types, where flow may also switch from one to the other, is termed as *transitional*. Factors that affect the type of cavity flow are the length-to-depth ratio of the cavity; the Mach number, the Reynolds number and the nature and state of the *approach boundary layer*.

Open cavity flows (that is the shorter length-to-depth ratios) are often unsteady. Rossiter's [3] semi-empirical model describes a feedback loop between vortex shedding and acoustic radiation, from the cavity front and rear. A modified version of this model is provided by Heller and Bliss [4]. Although successful in some cases, the validity of these formulae for high supersonic flows has been challenged [5,6].

Although numerous experimental and computational works have investigated cavity flows over a range of Mach numbers, our understanding of the cavity flow physics still remains incomplete. Such knowledge is critical to attempts to control or exploit such flows. Examples include reduction of noise and structural loading, in both aeronautical and non-aeronautical applications, and enhanced fuel and air mixing in hypersonic propulsion systems.

2 Cavity model and test conditions

The supersonic blow-down wind tunnel of the Aeronautics Department produces a nominal test-section Mach number of

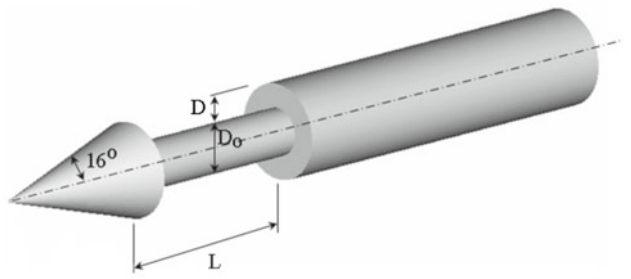

Fig. 1 Cavity model

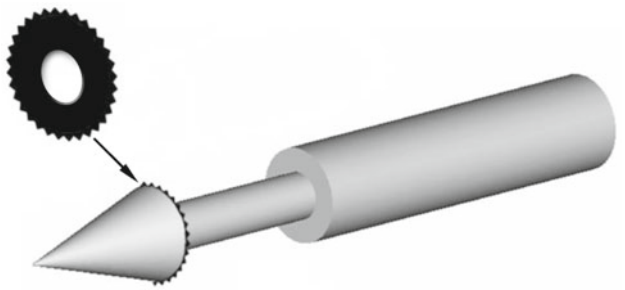

Fig. 2 Tripping disk used at the cavity front corner

Table 1 Flow properties in the supersonic wind tunnel

M_∞	p_∞ (Kpa)	T_∞ (K)	T_{wall} (K)	Re_∞ (/m)	$Re_{\infty,s}$
2.2	25.25	146.34	300	32×10^6	0.87×10^6

2.2 for a maximum run time of 20–30 s. The working section dimensions are 9.83×10^{-2} m in height by 10.15×10^{-2} m in width by 37.5×10^{-2} m in length, with a window for optical access that is approximately 96 mm in diameter. Experimental data acquisition comprised both schlieren visualisation, using an 8.0 Mega pixel digital camera together with a spark light source (spark duration of order 1 μs), and time-averaged surface pressure data.

The model consists of an axisymmetric configuration, following a long tradition in our Departmental high-speed research to employ bodies of revolution to produce time-averaged flow to the highest possible standards of two-dimensionality [7–11]. It comprises a rectangular-section annular cavity generated by the cone-cylinder configuration, as shown in Fig. 1. The cavity depth D (3 mm) and cone semi-apex angle (16°) and cone length (26.16 mm) are all fixed. The cavity length, L, may be varied between 3–37 mm to investigate dependence on the L/D ratio, by sliding the rear cylindrical section backwards on the central 'sting', diameter D_o (9 mm), which provides the cavity floor.

The wind tunnel free-stream conditions are presented in Table 1. The free-stream unit Reynolds number is $Re_\infty = 32 \times 10^6$ m^{-1} and $Re_{\infty,s}$ is the Reynolds number at the cavity front lip based on free-stream conditions and the wetted distance along the cone surface. At these conditions the flow is expected to be laminar on the fore-cone. The nature of transition in the free shear layer is unclear, however, and so some experiments employed the 'tripping' disc shown in Fig. 2.

3 Computational procedure and initial CFD results

CFD modelling used an in-house second-order-accurate code, formulated as two-dimensional axisymmetric, that has been successfully used in a wide range of compressible flow studies, including axisymmetric cavities [8–12]. Computations are presented here for cavities with L/D ratio of 1.33, 10.33, 11.33 and 12.33. For turbulent computations Menter's one-equation variant of the $\kappa - \epsilon$ model [13] is used, with transition forced at the cavity front corner whilst maintaining laminar flow on the conical fore-body. Walls are specified as isothermal at 300 K.

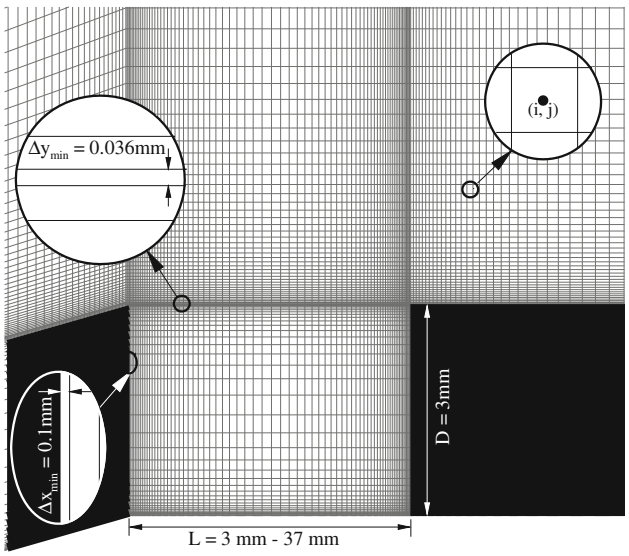

Fig. 3 Details of mesh used for computations. Flow is *left* to *right*

A typical mesh is shown in Fig. 3. The coarsest mesh comprises $10L$ cells along the cavity length (L, the cavity length in mm), and 50 cells to the cavity depth, D. Mesh refinement was achieved by doubling the number of cells in both directions, with a further doubling if necessary. The need to provide good resolution of the thin boundary layers, and the free shear layer developing over the cavity, required that the mesh be condensed around these regions using various stretching factors, as illustrated by Fig. 3. Cell centres and boundaries are identified by their (i, j) co-ordinates as shown.

Assessment of mesh convergence is not straightforward for flows that are highly unsteady and involved studying the evolution of surface skin friction with various mesh densities.

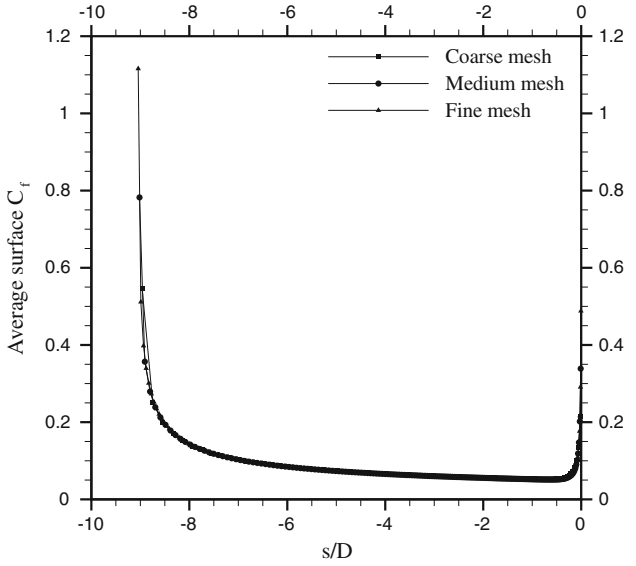

Fig. 4 Mesh convergence study results for fore-cone, laminar flow computations

This property was selected, rather than pressure, since it is strongly dependent on the correct resolution of the boundary layer and free shear layer and hence is a much more sensitive measure for assessment. The fore-cone flow is the most straightforward, since it is steady, but it is important to establish this first since it provides the initial conditions for the subsequent development of the free shear layer. The corresponding surface skin friction is plotted against wetted distance s/D($s/D = 0$ is the cavity front lip; $s/D \leq 0$ is the fore-cone) in Fig. 4 for all the three mesh levels, showing nearly perfect collapse. In all the computations laminar flow is computed over the conical fore-body. In the turbulent cavity computations turbulence is enforced at the cavity front lip.

The cavity flow itself can be unsteady, so that assessment for mesh dependence should strictly address some aspect of the time-resolved data. For the purpose of this work, however, we have looked at the dependence of the *time-averaged* flow properties on the mesh density. This is still a very demanding exercise and it has not been possible to carry this out for every cavity case. Assessment has been restricted to the shortest cavity ($L/D = 1.33$), for both the laminar and turbulent computations and for one of the longer cavity laminar flow cases.

Figures 5 and 6 show the time-averaged surface pressure and surface skin friction plotted against a wetted distance s/D for the $L/D = 1.33$ cavity, for the laminar and turbulent cases respectively. Here $0 \leq s/D \leq 1$ corresponds to the front face of the cavity, $1 \leq s/D \leq 2.33$ is the floor of the cavity and $2.33 \leq s/D \leq 3.33$ is the cavity back face. The data were obtained by running the computation for a sufficiently long time so that a stationary average was produced at the surface sample points.

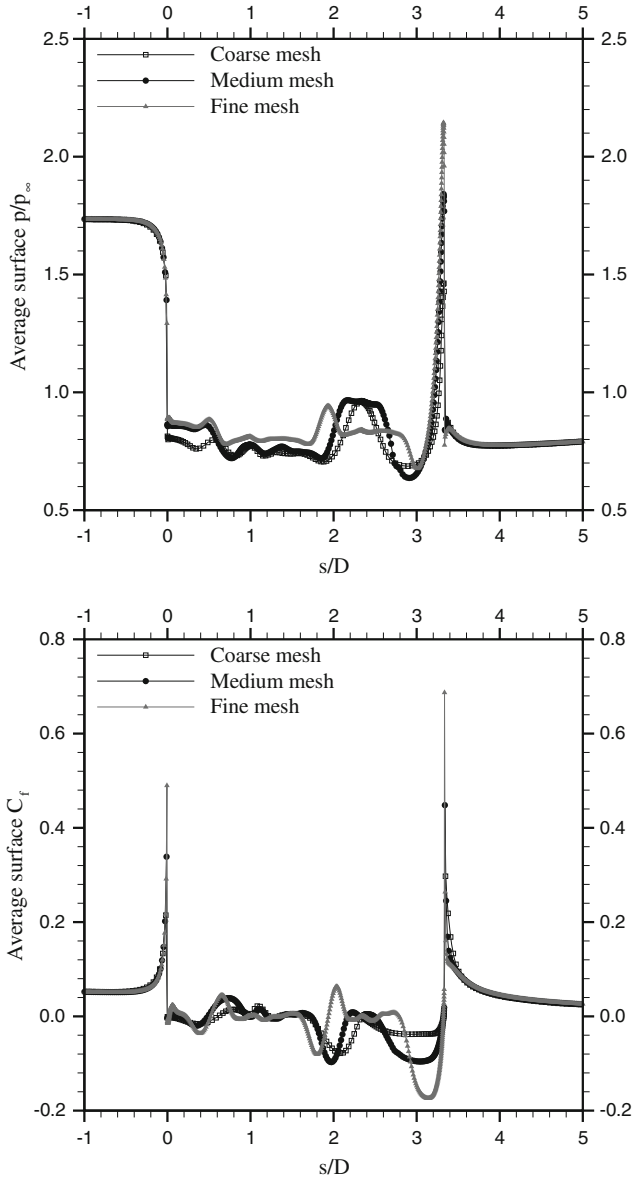

Fig. 5 Mesh convergence study for the short cavity, $L/D = 1.33$, laminar flow computations

The pressure and skin friction data show very rapid changes in the region $-0.2 \leq s/D \leq 0$. This is within about one boundary layer thickness, δ_{99}, of the upstream cavity corner ($\delta_{99} \approx 0.39$ mm, $\delta_{99}/D \approx 0.13$ where δ_{99} has been determined from the computed velocity field as the point where the velocity is 99 per cent of the local flow velocity outside the boundary layer). In this case the upstream influence through the subsonic part of the boundary layer permits the flow to accelerate in anticipation of the expansion corner and the cavity. This phenomenon was noted in the earlier cavity study of [8]. It is a real effect, difficult to measure experimentally because of the small physical space that it occupies, that is revealed progressively as the mesh refinement is increased.

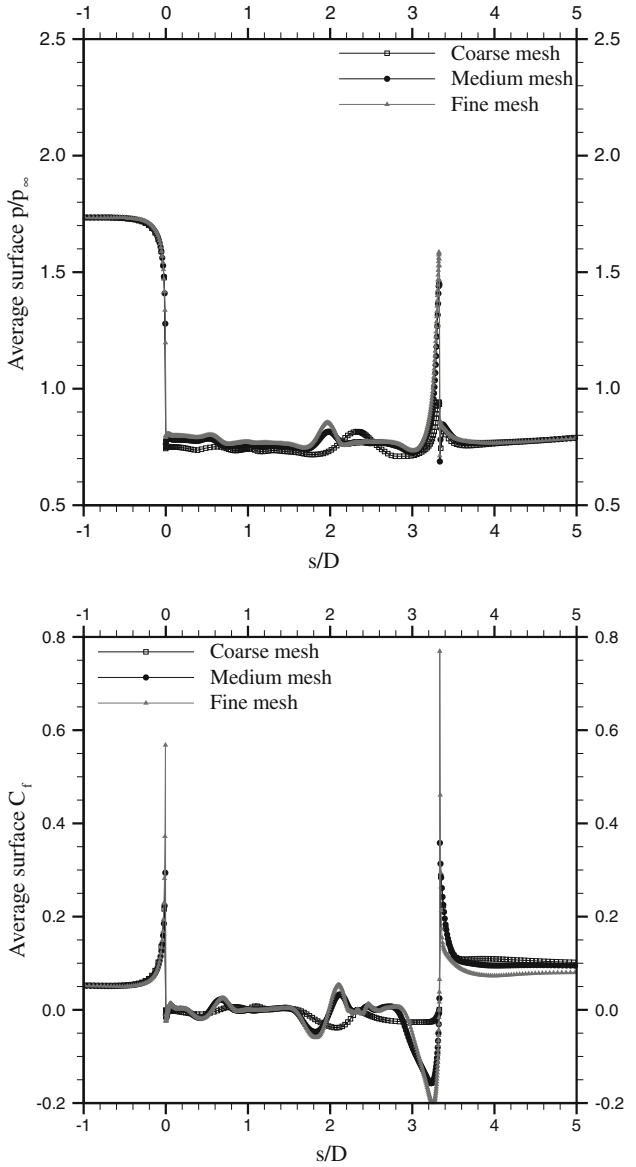

Fig. 6 Mesh convergence study for the short cavity, $L/D = 1.33$, turbulent flow computations

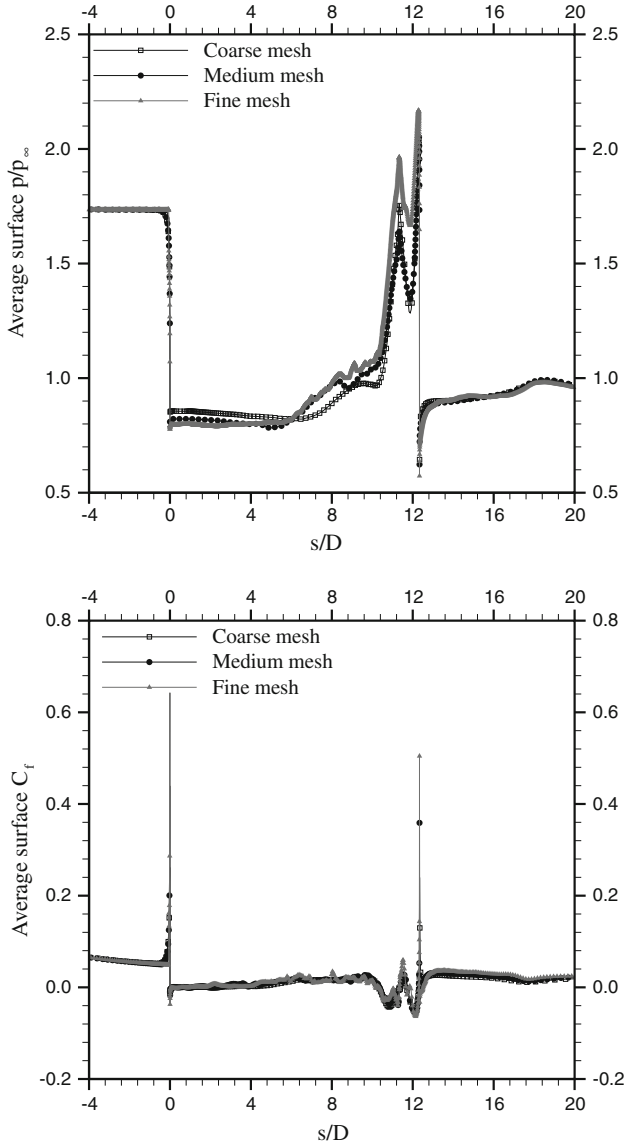

Fig. 7 Mesh convergence study for the long cavity, $L/D = 10.33$, laminar flow computations

A similar, singular-like, behaviour occurs in the vicinity of the rear lip of the cavity (at $s/D = 3.33$).

Within the cavity region Figs. 5 and 6 show that proof of mesh convergence has not been completely achieved, even for the finest mesh, but with the turbulent computation showing the better convergence of the two. The mesh refinement assessment for the longer (laminar flow) cavity, shown in Fig. 7, apparently provides better convergence compared with that of the $L/D = 1.33$ cavity. Often in CFD modelling for turbulent flows a criterion is invoked, for mesh convergence, based upon the minimum y^+ value for the 'wall cell'. This can be misleading for flows with severe pressure gradients, or flow reversal, certainly if a time-average definition is used. Locations such as separation and reattachment, with zero wall shear stress, give zero values for y^+, irrespective of the actual cell physical dimensions. Nonetheless, for Fig. 6, for example, the y^+ values of the wall cell (based on the wall-normal dimension of the cell and the surface value for density) give values at the mid-height of the cavity front face, mid-floor and mid-height of the cavity back face of 1.16, 2.2 and 0.87, respectively, for the finest mesh computation. For the corresponding locations for the longest cavity, $L/D = 12.33$, the y^+ values were 1.2, 1.5 and 7.2.

4 Experimental results and CFD code validation

Colour schlieren images (using a coloured filter rather than a knife edge) presented in Fig. 9 show the main flow features

such as the cone apex shock wave (in all cases) and re-attachment and re-separation shocks (for the closed cavities). The images were triggered manually using an exposure time of 1×10^{-6} s. The free stream flow speed is approximately 500 m/s in the supersonic region. This means that in the time the image is taken a flow particle in the supersonic region travels approximately 0.5 mm (e.g. $0.17D$ or $0.014L$ for the $L/D = 12.33$ cavity). Therefore, all the schlieren images are considered to be frozen. The schlieren pictures for each cavity were taken twice, once with the bare model and a second time with the tripping disk placed at the cavity front corner as shown in Fig. 2. Both sets of tests revealed that open cavity flow occurs for L/D values up to and including 11 and closed cavity flow occurs for L/D of 11.33 and above. Therefore, presence of the tripping disc did not alter the results in terms of re-attachment of the shear layer onto the cavity floor. This serves as additional support for the assumption that the shear layer, at least not too far downstream of the cavity front corner, is turbulent in the experiments and justifies the decision to force transition at the cavity front corner in the turbulent computations. The experimental schlieren images also clearly demonstrate the axisymmetry of the large-scale flow features.

Basically, the shortest cavity studied ($L/D = 1.33$) provides a free shear length that is only 15% of the fore-cone length. The expectation is that this cavity will be laminar. The longest cavities studied ranged $10.33 \geq L/D \geq 12.33$, and it was not possible to be categorical at the beginning of the study as to whether the flow should be laminar or turbulent. In consequence, these longer cavities were modelled both (a) as fully laminar and also (b) as laminar fore-body with free shear laser transition forced at the upstream cavity lip with a fully turbulent computation downstream. We will see later that laminar computations showed unsteady open cavity flow for the $L/D = 10.33$, which agrees with the experimental schlieren images of Fig. 9b whilst the turbulent computation also indicates unsteady open cavity flow, though with much reduced fluctuation amplitude. For the cavity lengths of $L/D = 11.33$ and 12.33 the laminar CFD shows unsteady transitional flow (in the sense of switching between open and closed cavity flows), whereas the experiments of Fig. 9c, d indicate closed cavities as also do the turbulent computations. For these long cavity cases we still present both laminar and turbulent CFD. The former because it provides insight into the general behaviour of transitional cavity flows and the latter because it provides by far the best agreement with the specific experimental data of this present study as shown in Figs. 8 and 10. The experimental time-averaged surface pressure data for the $L/D = 12.33$ cavity are compared with the CFD in Fig. 8. The cavity floor lies in the region $1.0 \leq s/D \leq 13.3$ and the experimental data show the scatter/repeatability associated with successive tests. The CFD has captured virtually all of the significant

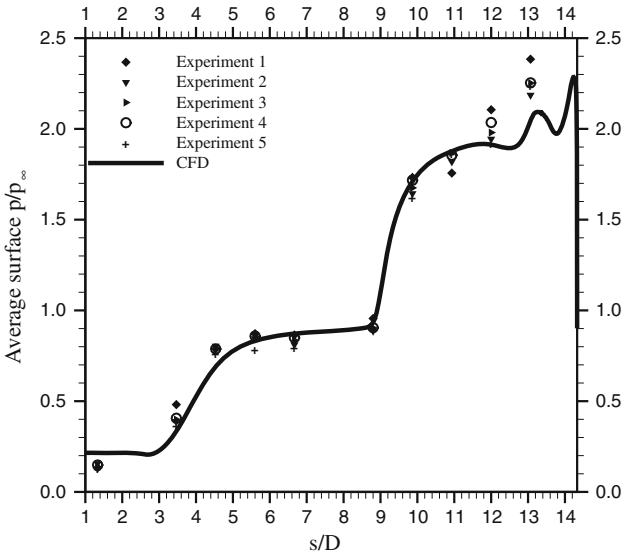

Fig. 8 Experimental and computational surface pressure variation on the closed cavity floor, $L/D = 12.33$, turbulent flow computation

features, including the pressure plateau regions and the rises in pressure, i.e. the regions of re-attachment and re-separation shocks. Figure 10 compares the experimental schlieren picture for the $L/D = 12.33$ cavity with a 'computational schlieren' (a horizontal knife edge for both experiment and CFD) using the program of Murray [14] to reduce appropriately the computed density field. A very close agreement is seen between CFD and experiment for the major wave locations and for the reattachment and re-separation positions on the cavity floor. These comparisons, schlieren and pressure, provide good supportive evidence for the quality of the CFD computations.

5 CFD results: laminar computations

5.1 Vortex convection and unsteady wave formation

Density contours, which highlight both pressure waves and also the shear layer and associated vortex systems, are presented in Fig. 11 for the laminar computations for cavities with L/D of 1.33, 10.33, 11.33 and 12.33. All the flows are unsteady, so that a single 'snapshot' of the instantaneous flow field is shown in each case, and all correspond to 'open' cavity flows. The shear layer disturbances, evident as vortex structures, convect downstream and stretch and distort as they negotiate the rear lip of the cavity and emerge onto the after-body. With increasing L/D, increasingly larger structures appear towards the rear wall.

There is a radical difference between the short and long cavities, with respect to the instantaneous flow development. Figure 12 shows a sequence of density snapshots together

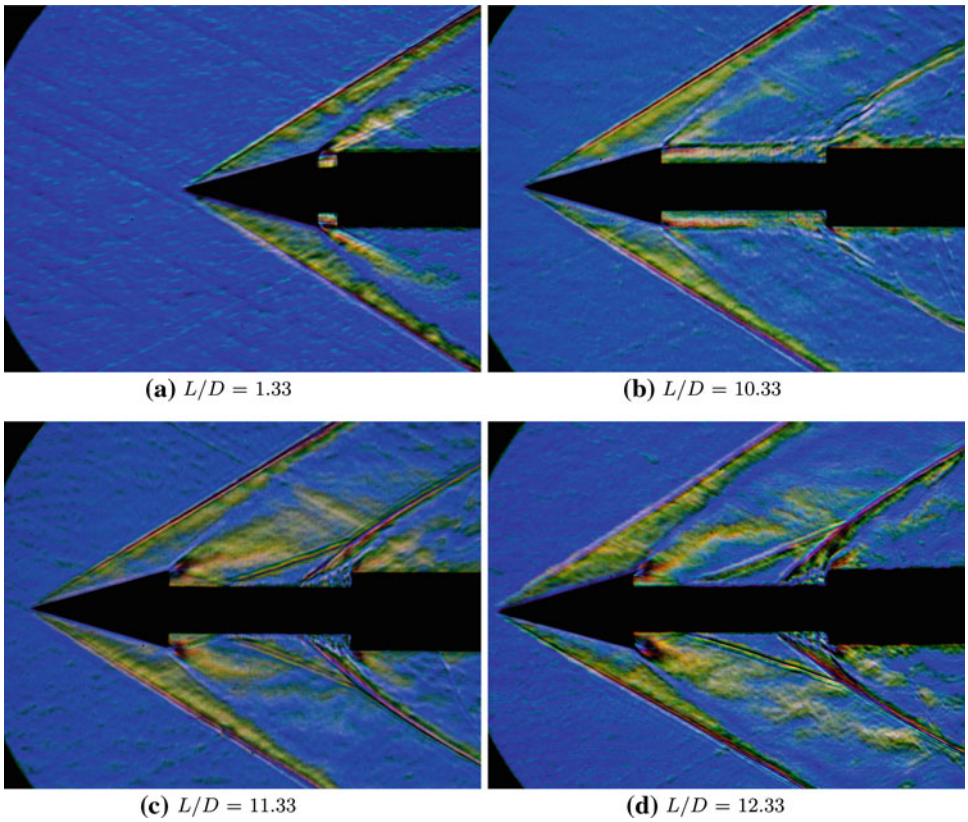

Fig. 9 Experimental schlieren visualisation images of various cavity cases

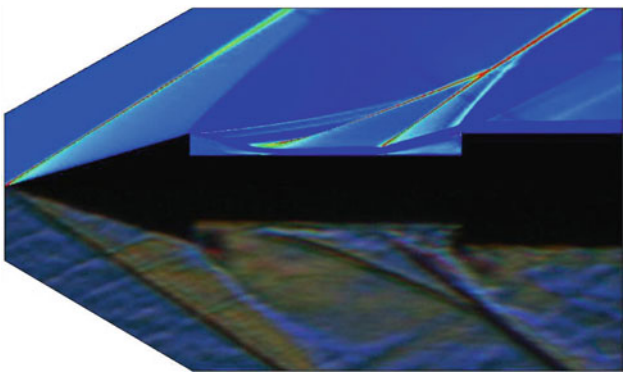

Fig. 10 Comparison between turbulent flow CFD (*top*) and experimental schlieren (*bottom*) for $L/D = 12.33$

with the instantaneous surface pressure distribution, for the $L/D = 1.33$ case, whilst Figs. 13 and 14 show the corresponding sequence for $L/D = 10.33$. The obvious visual difference is the (relatively) short wavelength structures formed over the length of the shear layer for the short cavity, and the apparently more quiescent initial development for the longer cavity where little obvious structure is seen until development lengths of order two cavity depths. In fact there is a long length-scale fluctuation for the long cavity. This can be seen by contrasting Figs. 15 and 16, for pressure histories at the front and back lip of the short cavity, with Figs. 18 and 19 for the longer case. Probably, the latter motion could be regarded as some type of shear layer 'flapping', characterised here by very abrupt increases in pressure that are followed by a more gradual, and noisy, fall.

Of course, the unsteady pressure wave formation depends upon the motion of the vortex systems along the whole length of the free shear layer (and downstream) and also on the associated unsteady motion in the cavity interior. The propagation behaviour of the resultant wave systems, their contribution to any cavity-oscillation feedback process, and their transmission to the external flow field, is necessarily complex. Above the shear layer—that is external to the cavity—the absolute Mach number is supersonic, so that the only pressure wave feedback path is via the cavity interior. The longer cavities show little indication of wave transmission to the front face from the back face, in direct contrast to the short cavity ($L/D = 1.33$), best seen in Fig. 20. In Fig. 20 a train of waves are seen to propagate within the cavity from back to front, with vigorous periodic pressure fluctuations at the cavity front and rear lips and middle of the cavity floor (Figs. 15, 16 and 17 respectively).

For the short cavity, not only is the wave train transmitted upstream through the cavity flow field but also wave fronts clearly then propagate out through the shear layer into the external flow. Although external waves cannot independently propagate upstream, the 'foot' of the external wave is 'dragged' upstream by the movement of its

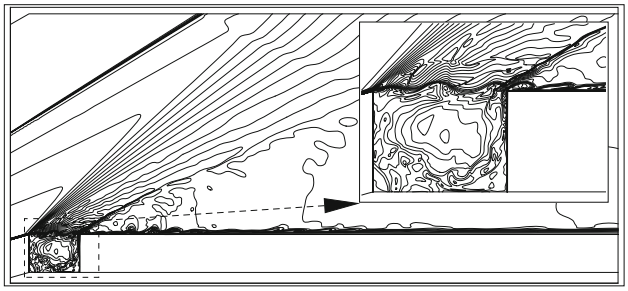

(a) $L/D = 1.33$

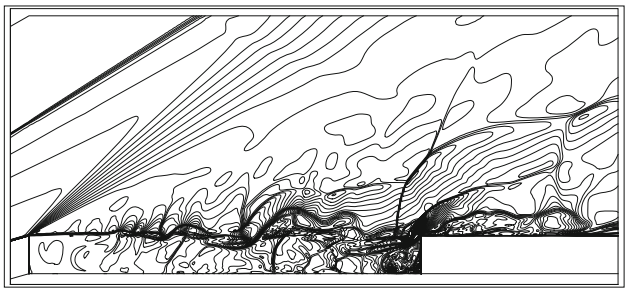

(b) $L/D = 10.33$

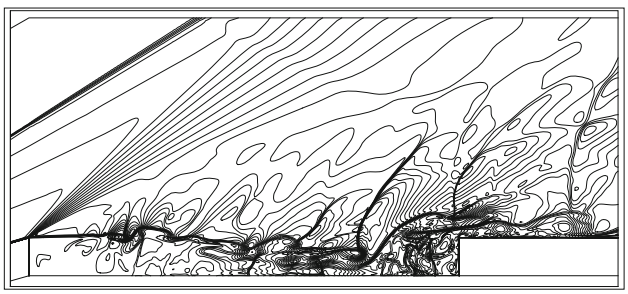

(c) $L/D = 11.33$

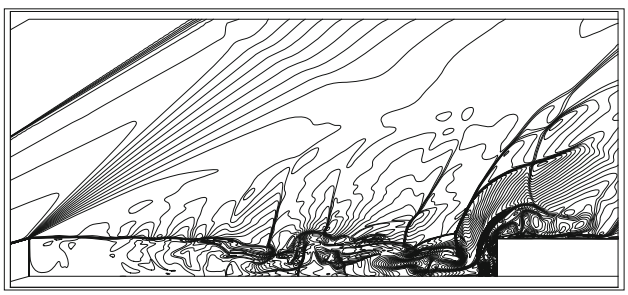

(d) $L/D = 12.33$

Fig. 11 Instantaneous density contours for laminar flow computations. ρ/ρ_∞ range is 0–2.5 for all, except for (**a**) $L/D = 1.33$ which shows 0–1.45, at 5% increments in ρ/ρ_∞ for all

'effective origin' in the shear layer. Such a mechanism would provide wave angles that are shallower than the external stream Mach angle. This can be clearly seen in Fig. 20 for example by comparing the highly swept and undulatory (because of the irregular nature of the shear layer) angle of the external waves above the shear layer with that of the trailing Mach line at the front lip expansion wave.

Figure 20 identifies clearly that the source for the pressure waves for the short cavity is the interaction of the shear layer vortex structures with the rear lip and wall of the cavity. The forward propagation of these waves is complex of course. They refract within the Mach number gradient of the cavity flow, reflect from the cavity walls (including reflection back from the front face) and floor, and propagate outwards through the shear layer as discussed previously. The shallow wave angles in Fig. 20, for the external radiation, are characteristic of the mechanism described above. For the long cavity, on the other hand, there are a distinct set of waves at steep angles, steeper than the fixed-frame external stream Mach angle and nearly normal to the flow direction. These waves are 'attached' to the vortex structures and convect downstream with them. That is, these waves are 'left-' or 'forward-' facing, but are moving downstream. This requires the relative flow between the external stream and the vortex structures to be supersonic, or at least sufficiently high that the flow becomes supercritical around the structures. In our case the relative Mach number appears to be just high enough for this to happen. Figures 13 and 14 show a sequence of snapshots, for vortex convection for the $L/D = 10.33$ cavity case, which provides a mean convection speed of $0.56U_\infty$. Given that the mean external velocity is approximately U_∞, the effective relative velocity of about $0.44U_\infty$ is sufficient to be supercritical or slightly supersonic. (We say 'effective', because the vortex structures grow in scale as they convect, so that the leading edge travels faster than the trailing edge and our estimate of convection speed is a value for the vortex 'centre'). In contrast, for the shortest cavity ($L/D = 1.33$), tracking the motion of the characteristic vortex structures, as shown typically in Fig. 12, gives a mean convection speed $U_c \approx 0.68U_\infty$ at the mid-cavity position. The velocity $\approx 0.32U_\infty$ relative to the external stream almost certainly means subsonic relative motion, explaining the apparent lack of any fixed connection between external waves and vortex structures. This is not a general result for short and long cavities, just a consequence in this specific case.

5.2 Shear layer roll up and oscillation cycle for cavity with $L/D = 1.33$

The flow structure inside the $L/D = 1.33$ cavity falls into a repetitive cyclical process that appears to be self-sustaining. This is illustrated by tracking one highlighted wave, W1, in the three consecutive instantaneous pressure contours shown for the $L/D = 1.33$ cavity in Fig. 20.

The flow unsteadiness is further illustrated in Figs. 15, 16 and 17 for the surface pressure time-history at the cavity front corner, back corner and middle of the cavity floor, for the $L/D = 1.33$ case. These show highly periodic oscillations of similar frequency at all three locations with a

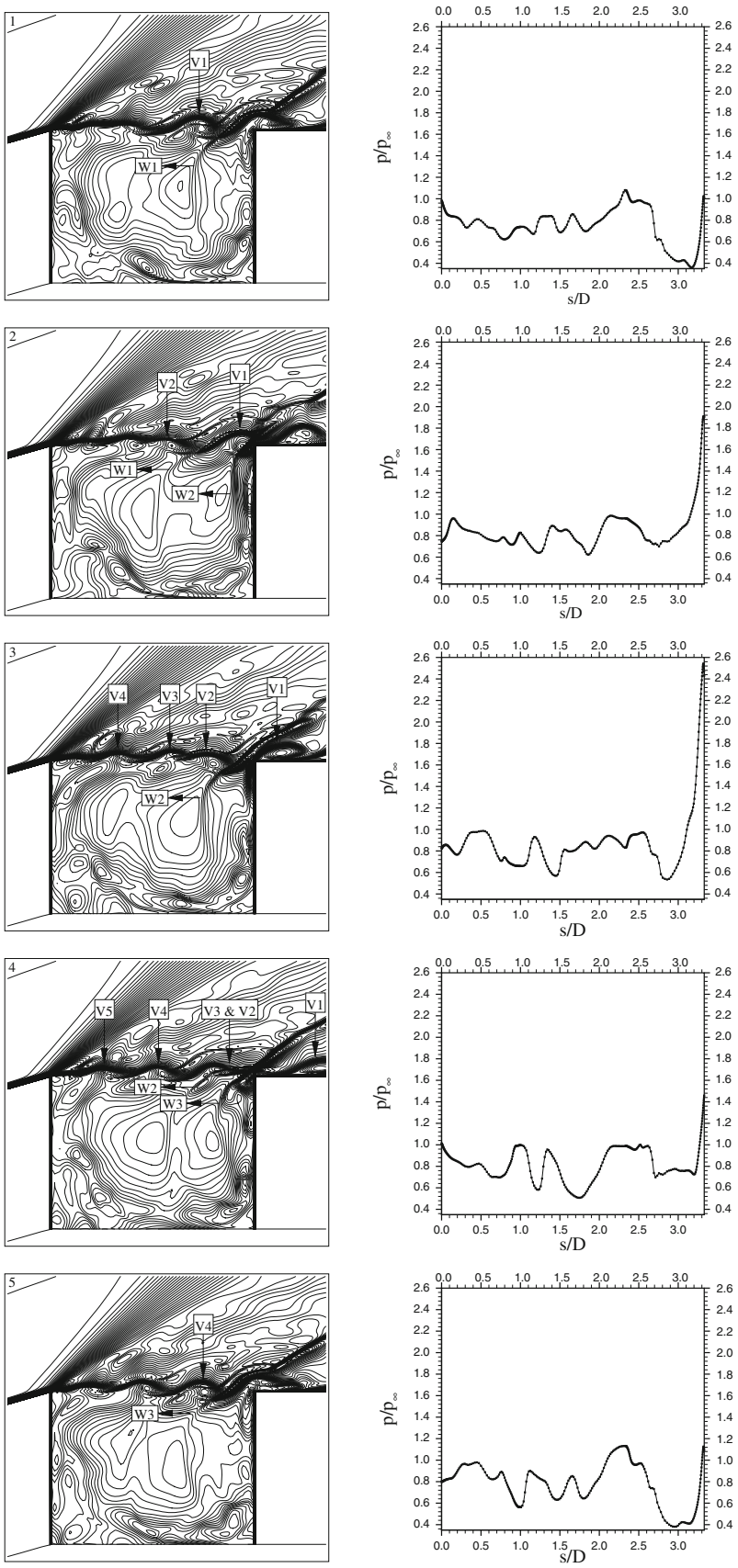

Fig. 12 Instantaneous density contours from laminar flow computations of $L/D = 1.33$ (*left*) and their corresponding surface pressures (*right*). ρ/ρ_∞ range is 0–1.5 at 2% increments in ρ/ρ_∞. Data presented at intervals of 0.44 in tU_∞/D

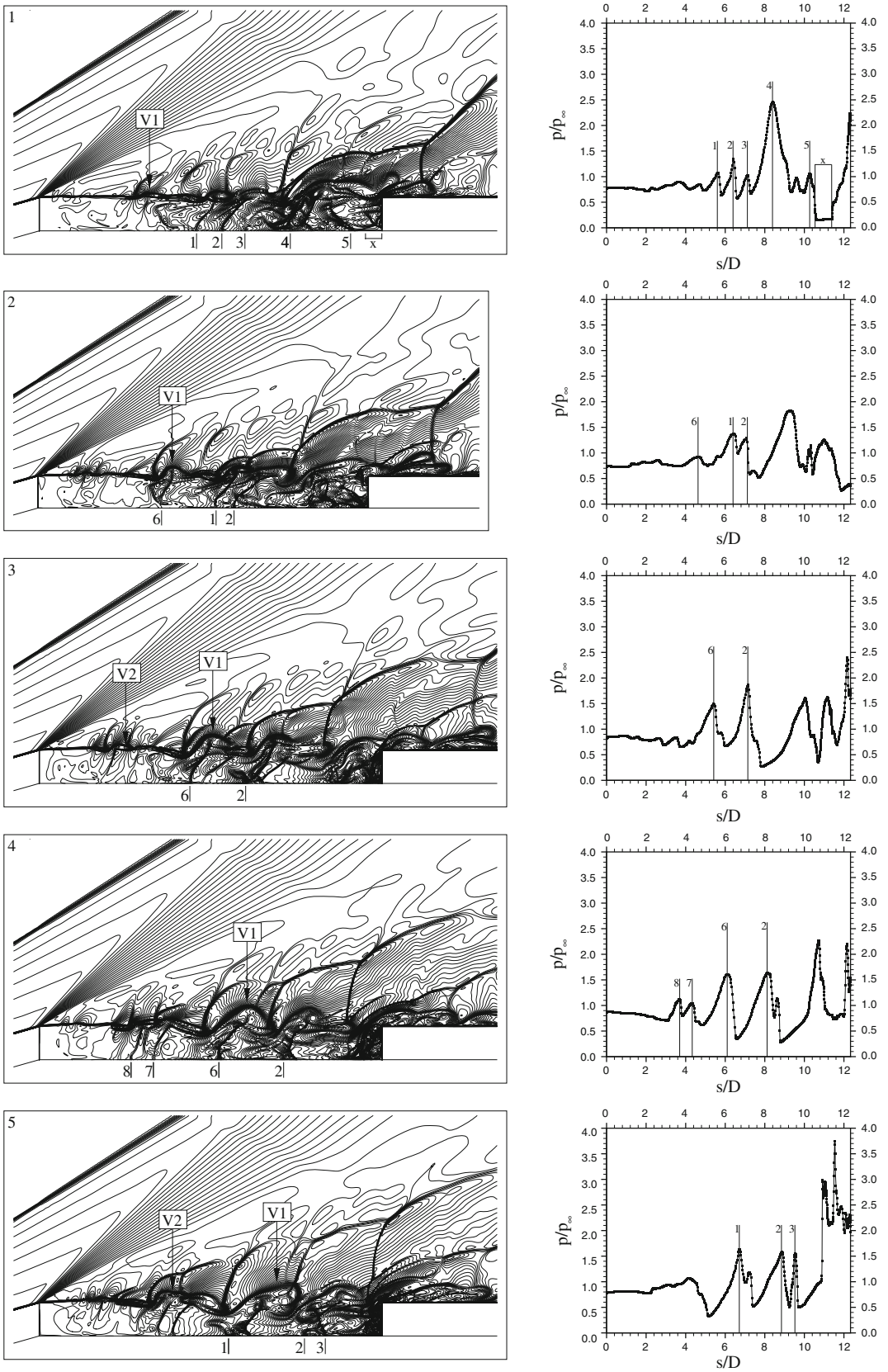

Fig. 13 Instantaneous density contours from laminar flow computations of $L/D = 10.33$ (*left*) and their corresponding surface pressures (*right*). ρ/ρ_∞ range is 0–1.8 at 3% increments in ρ/ρ_∞. Data presented at intervals of 1.78 in tU_∞/D

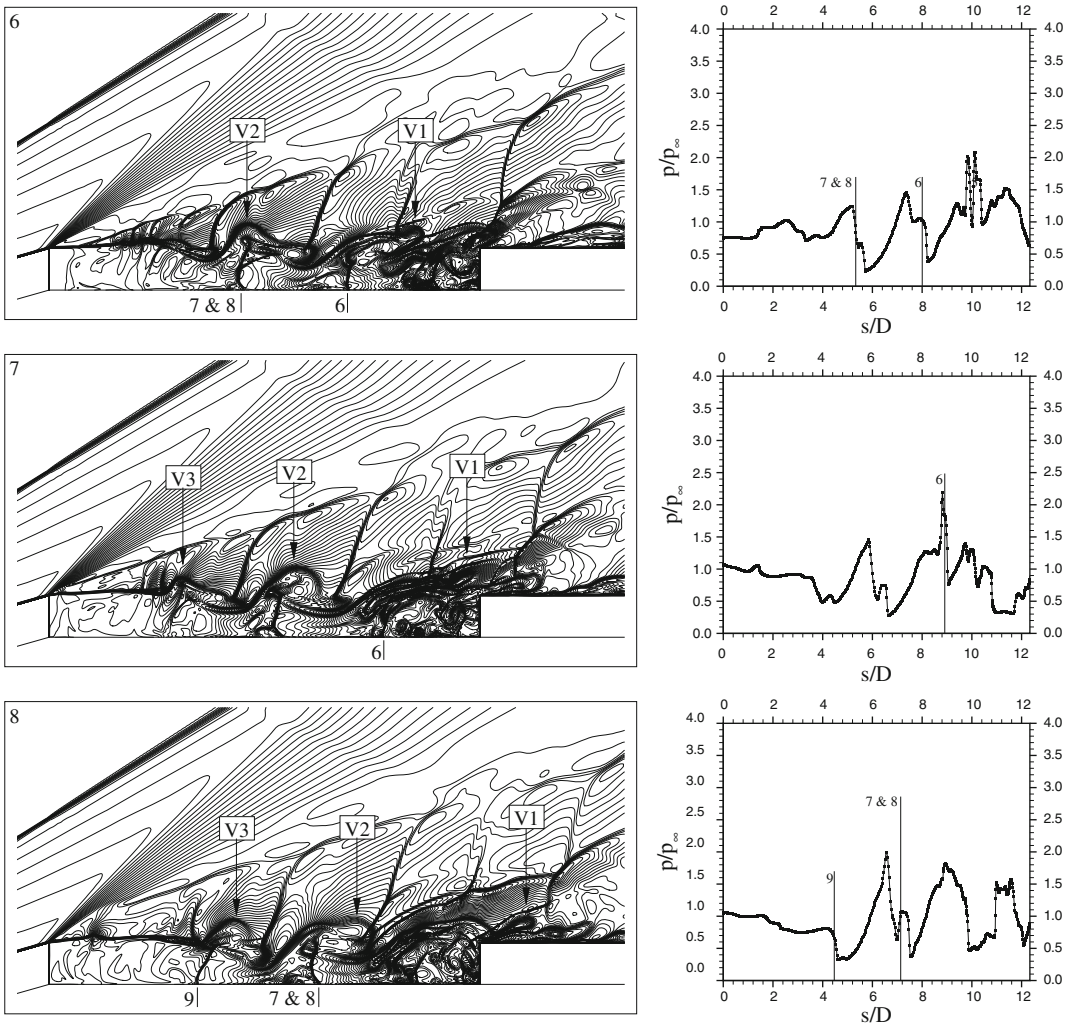

Fig. 14 Instantaneous density contours from laminar flow computations of $L/D = 10.33$ (*left*) and their corresponding surface pressure (*right*). ρ/ρ_∞ range is 0–1.8 at 3% increments in ρ/ρ_∞. Data presented at intervals of 1.78 in tU_∞/D

period of $tU_\infty/D \approx 0.66 (tU_\infty/L \approx 0.49)$ or $fD/U_\infty \approx 1.53 (fL/U_\infty \approx 2.03)$. Taking the characteristic vortex convection velocity as $U_{vortex}/U_\infty \approx 0.68$, as calculated earlier, it would take every vortex roughly $\Delta tU_\infty/L \approx 1.47$ to convect the entire length of the $L/D = 1.33$ cavity. This is probably an underestimate, because it does not include the vortex deceleration as it approaches the back face, but is already approximately three times greater than the timescale found above for the vortex shedding at the leading edge. Therefore, at any instant, we would expect to see three or more vortices simultaneously in the free shear layer, as is indeed seen in the instantaneous density contours of Fig. 12. This frequency is about six times larger than the basic 'feedback' cycle for the $L/D = 1.33$ cavity, corresponding to a single vortex convecting from front to back of the cavity, whose reflected sound wave then propagates upstream through the cavity to generate the next vortex. The higher frequencies encountered may therefore be a higher harmonic of this basic feedback cycle or due to some breakdown of the initial shear layer that actually has little dependence upon the cavity length. This was therefore explored further by a more systematic CFD investigation of several additional cavity cases.

5.3 Variation of cavity parameters around the basic case $L/D = 1.33$

For a *given* fore-body geometry and free stream conditions, the factors that can affect the behaviour are L, D, δ_{1e} (the boundary layer thickness at the cavity front lip) and D_o (the diameter of the cavity floor as shown in Fig. 1). In dimensionless terms the parameters are L/D, L/δ_{1e} (or D/δ_{1e}), D_o/D (or D_o/L). The cavity length, L, is the preferred scale for normalisation by the boundary layer thickness, since it is a direct measure of the shear layer development length. The cavity floor diameter, D_0, is best normalised by the cavity depth, D, since it can be regarded as some sort of measure

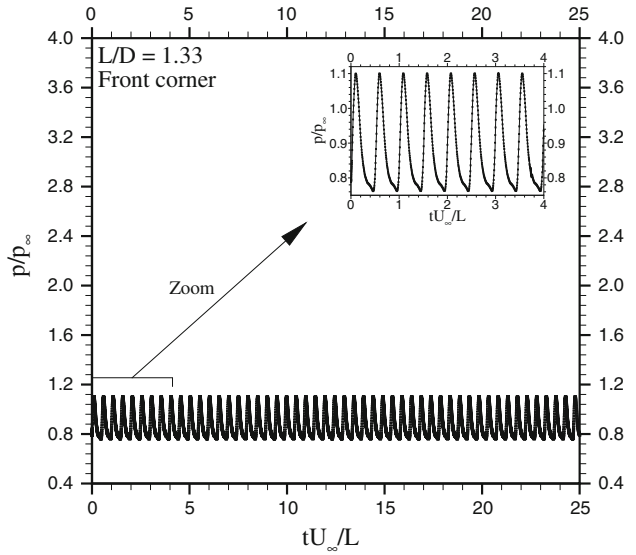

Fig. 15 CFD surface pressure time history at the front corner of the $L/D = 1.33$ cavity, laminar flow computation

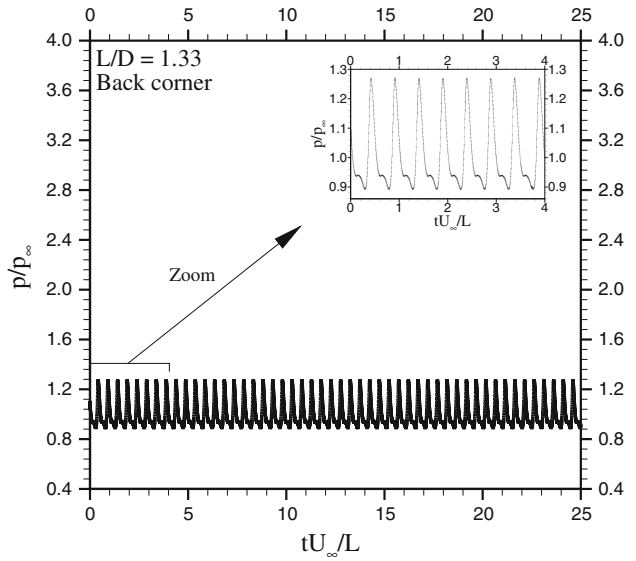

Fig. 16 CFD surface pressure time history at the back corner of the $L/D = 1.33$ cavity, laminar flow computation

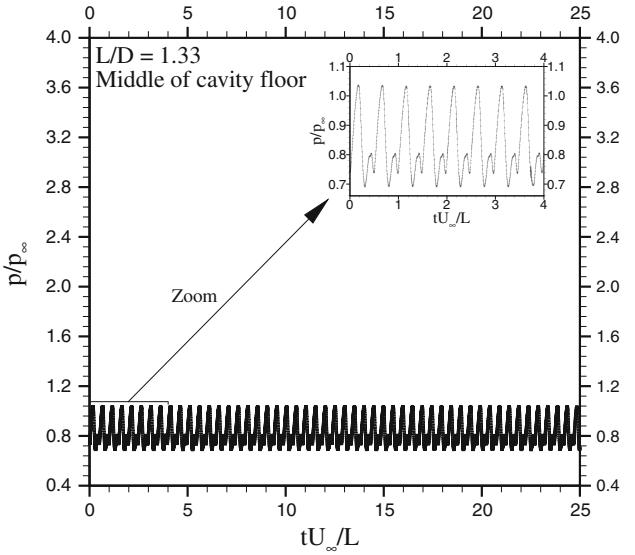

Fig. 17 CFD surface pressure time history on the mid-point of the $L/D = 1.33$ cavity floor, laminar flow computation

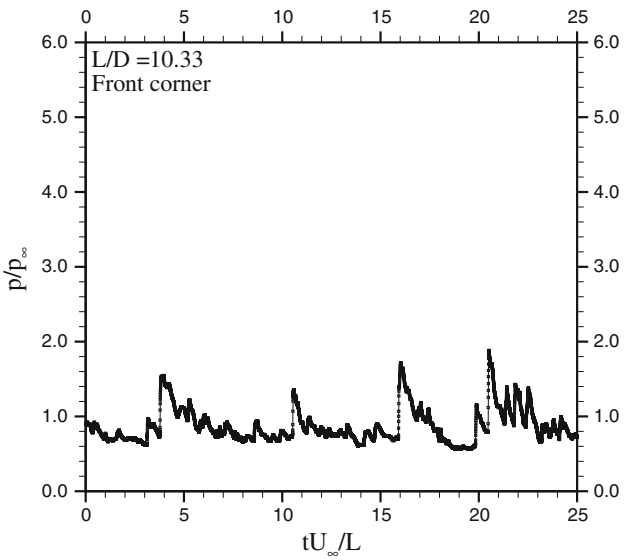

Fig. 18 CFD surface pressure time history at the front corner of the $L/D = 10.33$ cavity, laminar flow computation

for the tendency of the two-dimensional computations to tend to the planar limit (small values of D/D_0). The various cases computed are detailed in Table 2. They include doubling and halving of L and D, both separately and in combination. In addition, one computation where the unit Reynolds number was reduced by a factor of 4 to double the thickness of the fore-body boundary layer was carried out (see Fig. 21 for boundary layer profiles on the fore-body just upstream of the cavity front lip for both unit Reynolds numbers). In each case the computed surface pressure time-history at the front 'separation lip' of the computed cavities was monitored and the corresponding pressure histories are presented in Fig. 22. In those cases where a clear periodic frequency was detected the values are entered into Table 2. In other cases detection is less clear and no entry is made. Table 2 implies a rather complex dependence of the oscillation frequency upon L, D and the Reynolds number.

The first four cases correspond to the $L/D = 1.33$ cavity, and it is clear that the dimensionless frequency (fD/U_∞ or fL/U_∞) varies significantly between them, indeed also that the case with the largest values of L and D does not show the clear periodicity of the other three. Clearly the connection between cavity length and frequency is weak. The halving of cavity length between cases 1 and 3 leads only to a slight

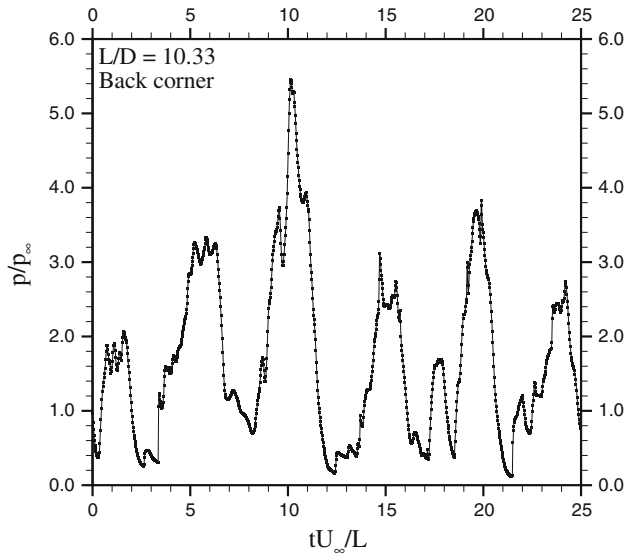

Fig. 19 CFD surface pressure time history at the back corner of the $L/D = 10.33$ cavity, laminar flow computation

increase in frequency (313 kHz as opposed to 271 kHz) rather than a doubling if the critical parameter were solely the cavity L/D ratio. This near independence from cavity length suggests that the periodicity results from the Kelvin–Helmholtz instability and that it is a natural consequence of shedding of the cone boundary layer from the front corner. The role of the upstream pressure waves that reach the front corner could be to provide the continuous disturbance environment to sustain the instability. Indeed, Kelvin–Helmholtz frequencies fall with increased shear layer thickness, so that the slight reduction in frequency between Case 3 and Case 1 may well be symptomatic of the longer shear layer development length. Hence, the latter case has a slightly thicker final shear layer. To explore this point further, the original $L/D = 1.33$ cavity has been computed with the unit Reynolds number reduced by a factor of 4. This doubles the initial boundary layer thickness, see Fig. 21 (which would also make the value of L/δ_{1e} the same as for the L and D halved case). The frequency is $f = 194.4$ kHz (see Fig. 22 for the pressure fluctuations at the front corner), significantly reduced from the basic case, and in line with the expectations that the Kelvin–Helmholtz frequency should reduce with increased shear layer thickness. Table 2 also includes the *time-averaged* pressures at the top of the front (p_F) and back (p_B) faces of the cavity, just below the cavity lip. A clear systematic reduction in pressure from Case 2 (L and D doubled), through Case 1 (the 'standard case') to Case 3 (L and D halved) can be seen. The values of both L/δ_{1e} and D/D_0 are changing with these three cases. The changes associated with the sequence would correspond either to the boundary layer, at separation, looking 'increasingly thick' compared with the scale of the cavity (essentially a Reynolds number effect) or the

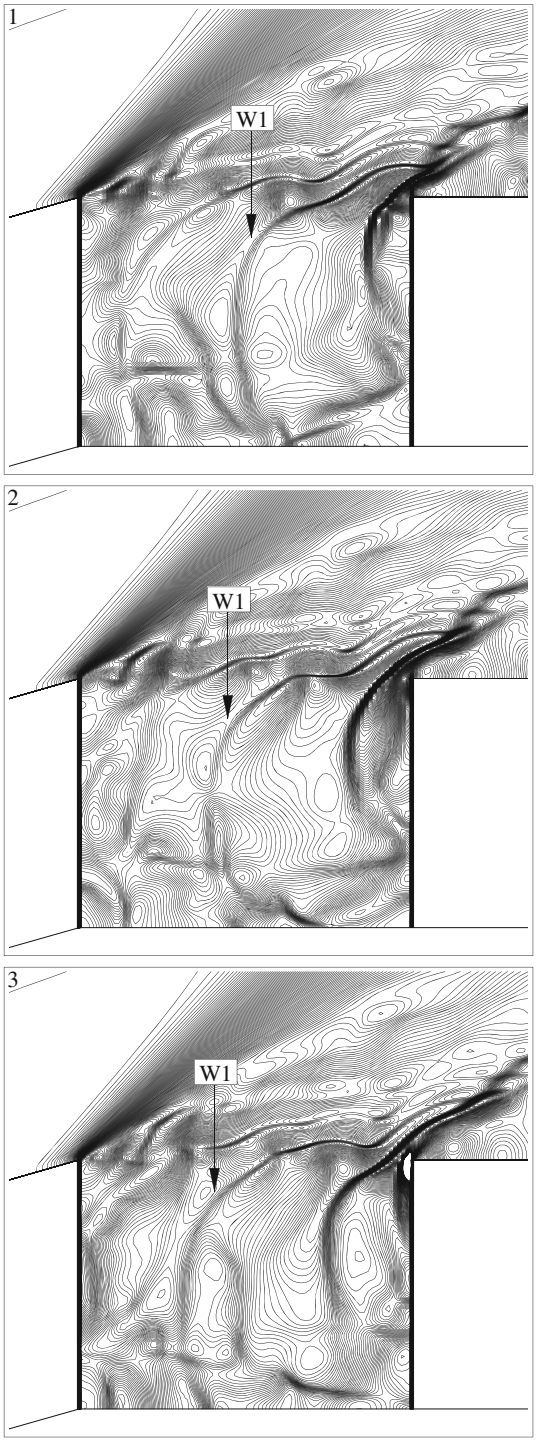

Fig. 20 $L/D = 1.33$ cavity instantaneous pressure contours. p/p_∞ is 0–1.7, at 1% increment, laminar flow computation

flow looking 'increasingly planar'. The strong variation of p_F and p_B can be better argued to be a consequence of the variation in L/δ_{1e} than in D/D_0. The underlying reason relates to effect of the initial boundary layer (on the forebody) on the development of the laminar free shear layer

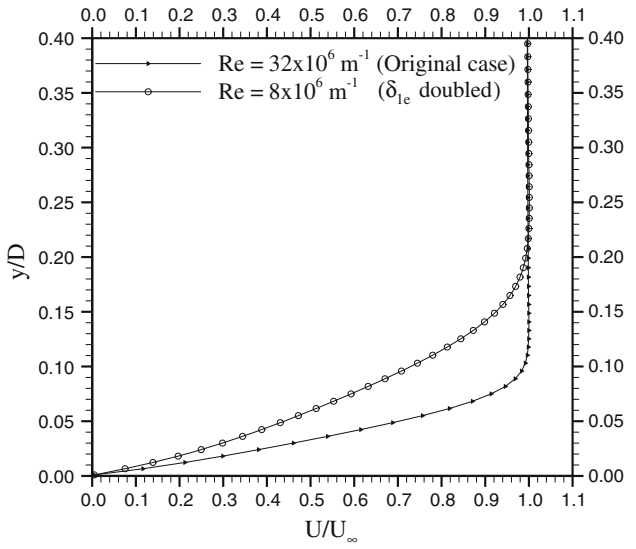

Fig. 21 Laminar boundary layer profile at the cavity front lip for the original and δ_{1e} doubled cases

downstream of the separation lip. References [15,16] and [17], amongst others, showed that large development distances are required to reach an asymptotic profile so that in most practical problems, the current one included, the shear layer is in a non-self-similar growth process. In this asymptotic state, with other provisos such as steady flow and a thin shear layer compared with the cavity depth, we would expect the mean reattachment pressure to be comparable to the stagnation pressure on the dividing streamline for a fully developed shear layer. Shorter development lengths would correspond to the dividing streamline lying 'lower' in the free shear layer, so that the corresponding stagnation pressure would be lower as well. This is a very complex issue, because the shear layer development is unsteady. Nonetheless, it is illustrated in part by the time-averaged streamlines for the original $L/D = 1.33$ cavity super-imposed onto a plot of the velocity vectors along the cavity length as shown in Fig. 23. The dividing streamline—the mean streamline from the separation lip to reattachment—is shown. The effect of the development of a new shear under the separation boundary layer is to shift the streamline to higher velocities, within the profile, for increased shear layer development distance. The longer that the shear layer has to develop, compared with the initial boundary layer thickness, that is the larger the value of L/δ_{1e}, then the higher this velocity and the higher the reattachment pressure. In turn, the re-attachment pressure helps pressurise the whole cavity. Therefore, higher pressures at re-attachment, which occurred for longer cavity lengths as shown, would result in higher pressures at the front corner, as tends to be shown in the table.

The other cases in Table 2 do not correspond to the $L/D = 1.33$ cavity. They were performed, in an effort to make sense of the mean pressure and oscillation frequency results, of cases 1 to 4, by exploring the effects of increasing and reducing the cavity length.

Halving the cavity length, but retaining the same depth so that $L/D = 0.67$, Fig. 22 and Case 5 in Table 2 show that the frequency of oscillation at the front corner ($f D/U_\infty \approx 1.34$) is little different from that found for the $L/D = 1.33$ case ($f D/U_\infty \approx 1.52$) in Fig. 15. Therefore, once again the oscillations at the front corner are not directly connected with the cavity length, where a halving of the cavity length might be expected to lead to an effective doubling of frequency for a simple feedback process rather than the slight reduction actually found. The same value of L/D can be produced by taking the basic case and doubling the cavity depth (Case 6), but a significant frequency and amplitude modulation indicates a significant departure from clear periodicity.

Next we look at the cases where $L/D = 2.67$. Both are irregular. The L-doubled case which can be regarded as either 'more axisymmetric', or has a longer shear layer development length, than the D-halved case (cases 7 and 8 in Table 2 respectively) is more irregular, see also Fig. 22; this is similar to the trend found for the $L/D = 1.33$ cavity (comparing cases 2 and 3) and the $L/D = 0.67$ cavity of case 6. With case 8, despite the significant amplitude modulation (noticeably more so in the positive-going pressure excursion rather than negative-going sense), the characteristic frequency, for the same shear layer development length as Case 1, is very substantially less, by a factor of nearly 4. It is difficult to argue this trend from the viewpoint of Kelvin–Helmholtz. However, it should also be recognised that this L/D cavity ratio must correspond to a change in the basic *mean* vortex structure in the cavity, essentially changing from one dominant vortex to two (see [8]) and hence a basic change in the flow field structure.

6 CFD results: turbulent computations

Figure 24 shows the turbulent computations for $L/D = 1.33$, 10.33, $L/D = 11.33$ and 12.33, equivalent to the laminar computations of Fig. 11. The results exhibit unsteady open cavity flows for $L/D = 1.33$ and 10.33 so that the images for these two cases are instantaneous snapshots. For both $L/D = 11.33$ and 12.33, the time-dependent computation converged to steady closed cavity flows are shown. This result is consistent with the experimental schlieren images of Fig. 9 and the excellent agreement with experiment, for the longest cavity, has already been commented on for Figs. 8 and 10. According to the CFD results, once the shear layer reattaches onto the cavity floor in the closed cavity case both the forward and rearward separation regions are steady. In Fig. 8 the two regions of pressure rise, for $3 \leq s/D \leq 5$ and $9 \leq s/D \leq 11$, near the cavity front and back faces, respectively, represent the location of re-attachment and re-separation shock waves inside the cavity.

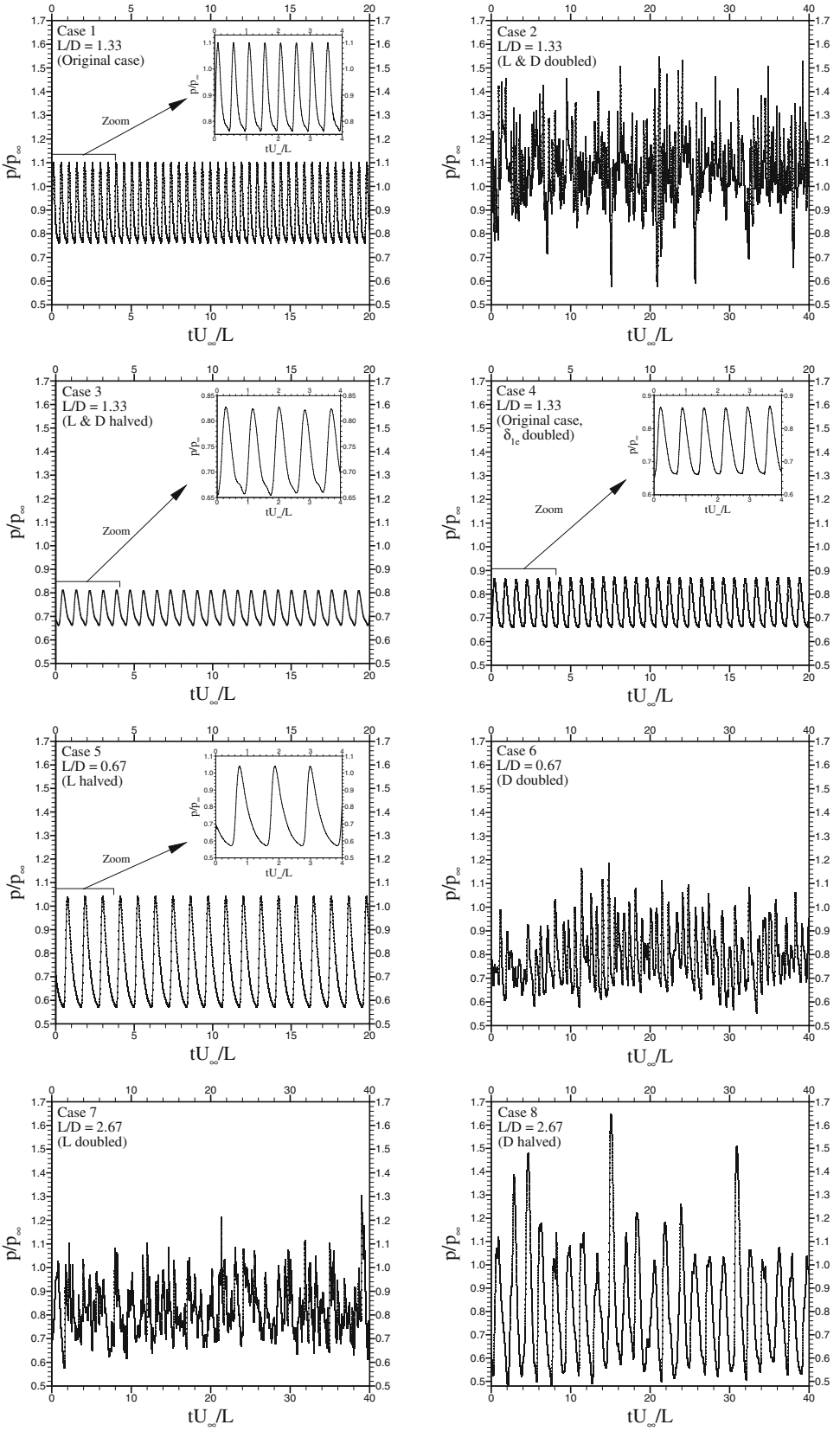

Fig. 22 Surface pressure time history at the front corner, for various cavity lengths and depths, for laminar flow computation of short open cavities

Table 2 Surface pressure oscillations obtained at the front corner of cavities with varying lengths and depths

Case	Parameter altered	L (mm)	D (mm)	δ_{1e} (mm)	R_0 (mm)	L/D	L/δ_{1e}	D/D_0	f (kHz)	fL/U_∞	fD/U_∞	p_F/p_∞	p_B/p_∞
1	N/A	4	3	0.27	4.21	1.33	14.8	0.712	270.5	2.03	1.52	0.88	1.9
2	L & D (x2)	8	6	0.27	1.21	1.33	29.6	4.96	–	–	–	1.06	2.4
3	L & D (x0.5)	2	1.5	0.27	5.71	1.33	7.4	0.263	312.6	1.17	0.88	0.72	1.01
4	L/δ_{1e}	4	3	0.54	4.21	1.33	7.4	0.712	194.4	1.46	1.09	0.75	1.13
5	L (x0.5)	2	3	0.27	4.21	0.67	7.4	0.712	238.1	0.89	1.34	0.74	0.72
6	D (x2)	4	6	0.27	1.21	0.67	14.8	4.96	–	–	–	0.78	0.83
7	L (x2)	8	3	0.27	4.21	2.67	29.6	0.712	–	–	–	0.82	0.75
8	D (x0.5)	4	1.5	0.27	5.71	2.67	14.8	0.263	75.0	0.563	0.21	0.81	0.83

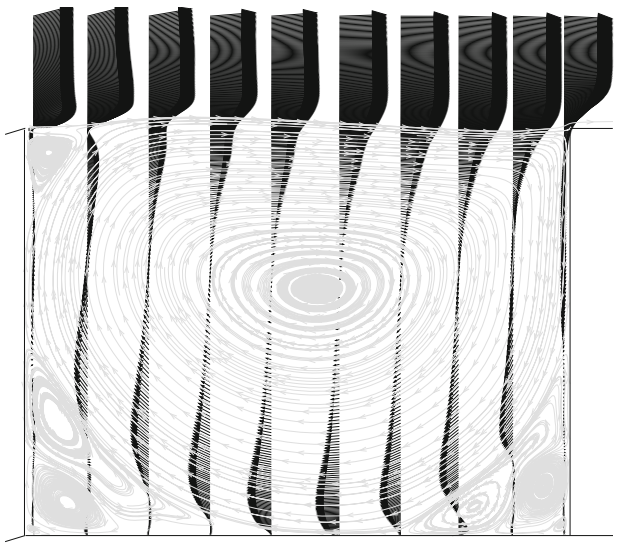

Fig. 23 Time-average streamlines inside the original $L/D = 1.33$ cavity and the velocity vectors along the cavity length, laminar flow computation

6.1 Comparison between turbulent and laminar computations

Figures 25 and 26 show the surface pressure histories for the front and back corners of the $L/D = 1.33$ cavity for the turbulent computation. Comparing these to their laminar counterparts, in Figs. 15 and 16, there is a more complex, modulated wave form for the turbulent case with highest frequencies comparable to those of the laminar computation, identifying again the probable importance of the Kelvin–Helmholtz instability, but with much severer fluctuation amplitudes for impingement/reattachment on the back corner of the cavity.

Rossiter's [3] original expression for a cavity feedback loop (forward-propagating vortex and rearward-moving pressure wave) gave an oscillation frequency, f_n, as

$$\frac{f_n L}{U_e} = \frac{n - \alpha}{M_e + 1/k} \tag{1}$$

where M_e and U_e are the Mach number and stream velocity above the free shear layer. These values are very close to the free stream values, taken as 1.75 and $0.88U_\infty$, respectively. The reciprocal of Eq. 1 gives the corresponding period for the cycle. In Rossiter's expression, k is the ratio of vortex convection speed to edge velocity, which we established earlier as 0.68, α is a factor (which Rossiter took as 0.25) to account for the time delay between the arrival of a vortex structure at the back face and the resultant emission of a sound wave, and n is the mode number. For our cavity, taking the fundamental value $n = 1$, Rossiter's model provides $\frac{f_n L}{U_e} \approx 0.2$ or cycle time T_n as $\frac{U_e}{f_n L} \approx 5.0$. As commented earlier, for our study this provides too low a frequency, and too large a cycle time, compared with values from our computation. Indeed, we require a mode number between 7 and 8 to best fit the data, which really stretches the model behind the theory. Additionally, appropriate values of the empirical constants α and k, and their dependence on flow conditions and L/D are not clear. They are often determined using a best fit to experimental data. Whilst the values $k = 0.57$ and $\alpha = 0.25$ gave the best fit to Rossiter's data, which covered a Mach number range of 0.4–1.2, in other work that cover Mach numbers up to 2.5 a range of values for k are reported, from 0.5 up to 0.75 [6,22]. Additionally, Tam et al. point out that Rossiter's equation does not always agree with data obtained for flows with Mach numbers outside the range 0.4–1.2 [5].

The surface pressure oscillations at the front and back corners of the turbulent $L/D = 10.33$ are presented in Figs. 27 and 28. In contrast to the short cavity, it can be seen that the pressure fluctuation amplitude, at both front and rear lips of the cavity, is much smaller in the turbulent case compared with the laminar case. For this turbulent computation, the transition from open to closed cavity appears to be relatively smooth compared with the laminar case.

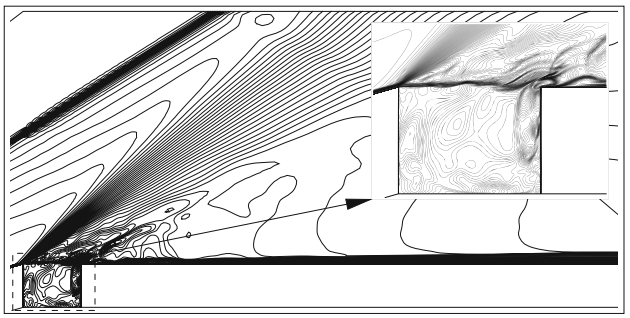

(a) $L/D = 1.33$

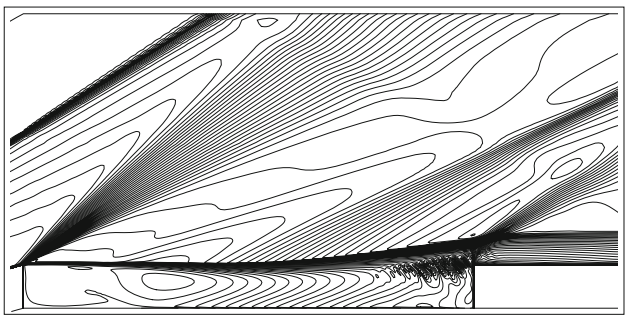

(b) $L/D = 10.33$

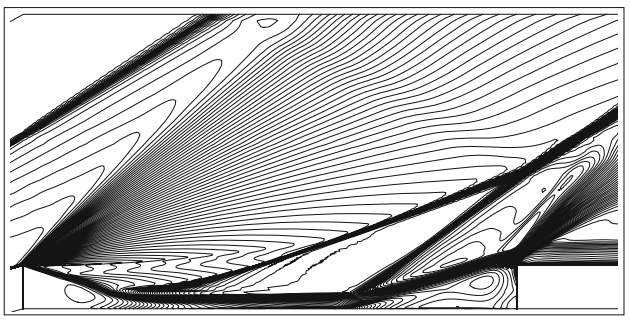

(c) $L/D = 11.33$

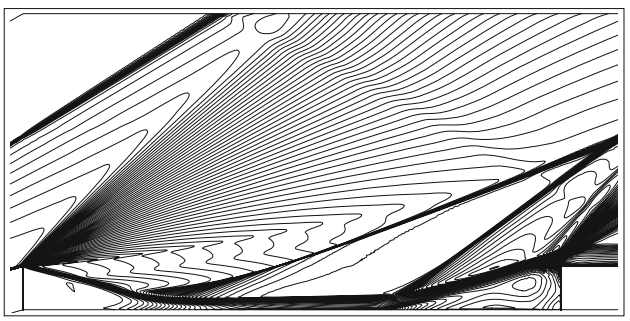

(d) $L/D = 12.33$

Fig. 24 Density contours for turbulent flow computations. ρ/ρ_∞ range is 0–1.5 at 1% increments for $L/D = 1.33$ and 10.33, and 0–1.6 at 2% increments for $L/D = 11.33$ and 12.33

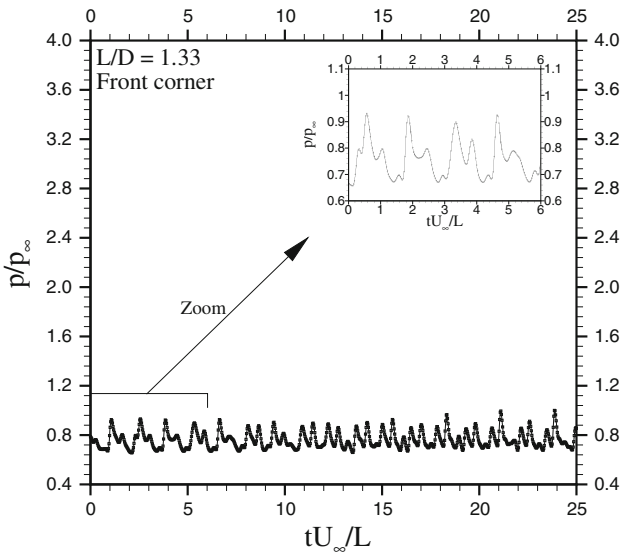

Fig. 25 CFD surface pressure time history at the front corner of the $L/D = 1.33$ cavity, turbulent flow computation

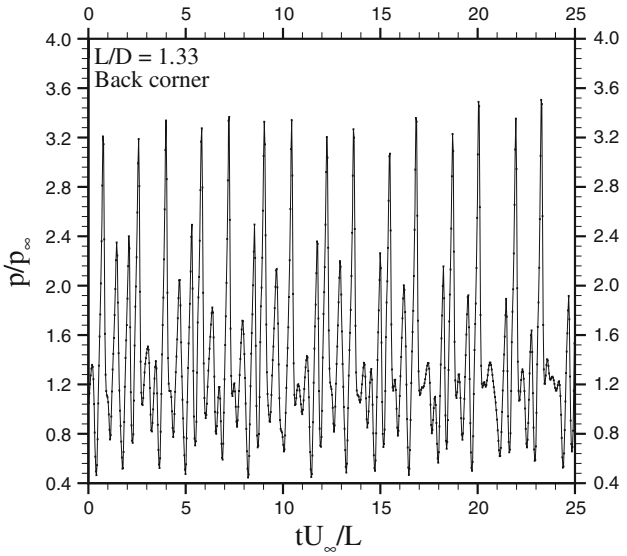

Fig. 26 CFD surface pressure time history at the back corner of the $L/D = 1.33$ cavity, turbulent flow computation

7 Concluding remarks

The laminar results for length-to-depth ratios of 1.33, 10.33, 11.33 and 12.33 all demonstrated unsteady open cavity flows, highly periodic for the shorter cavities ($L/D \leq 1.33$). Most of the evidence points to the likely cause as a Kelvin–Helmholtz instability, of the separating free shear layer, rather than a feedback process based on the cavity length which is the basis of the Rossiter model. However, the excitation of this instability will be linked with the pressure disturbance field, which of course is linked in turn to vortex structures interacting with the cavity flow, with each other and with their impact upon the cavity rear face and lip.

Turbulent computations carried out on the same cavities reveal that the flow switches from open to closed type for $L/D \geq 11.33$, which is consistent with the experimental

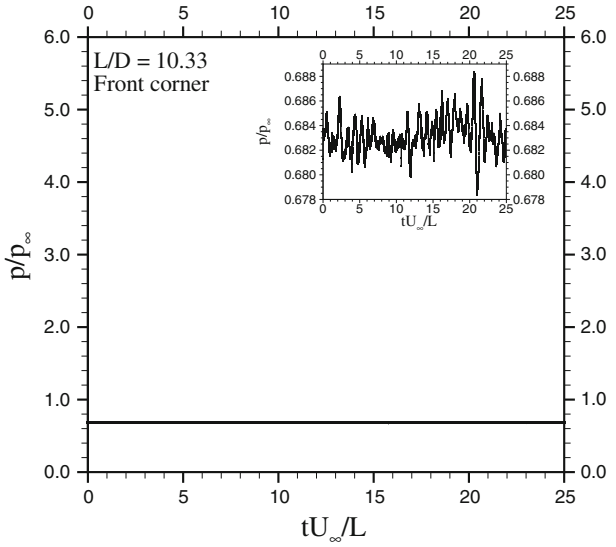

Fig. 27 CFD surface pressure time history at the front corner of the $L/D = 10.33$ cavity, turbulent flow computation

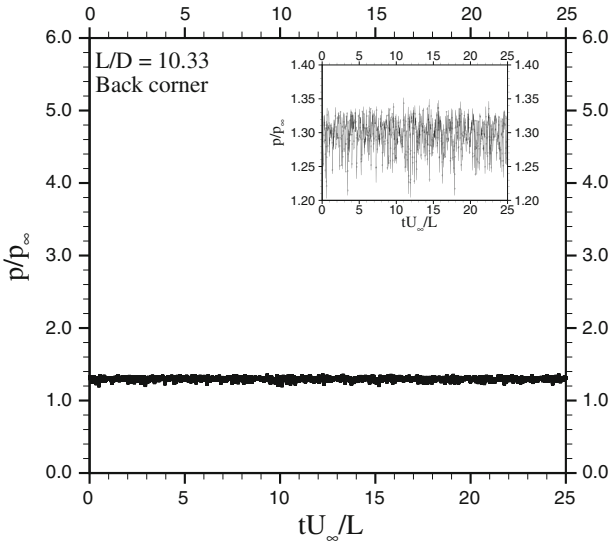

Fig. 28 CFD surface pressure time history at the back corner of the $L/D = 10.33$ cavity, turbulent flow computation

schlieren images. The time-averaged surface pressure data from experiment also agree well with the CFD. All computations, so far, have been two-dimensional (axisymmetric) and further work is focussed on investigating the importance of three-dimensionality.

Acknowledgments KM was supported by a studentship from the Engineering and Physical Sciences Research Council.

References

1. Dissimile, P.J.: Effect of planform aspect ratio on flow oscillations in rectangular cavities. J. Fluids Eng. **122**, 32–38 (2000)
2. Stallings, R.L.: Experimental cavity pressure distribution at supersonic speeds. NASA technical paper 2683 (1987)
3. Rossiter, J.E.: Wind-tunnel experiments on flow over rectangular cavities at subsonic and transonic speeds. Aeronautical Research Council technical paper 3438 (1964)
4. Heller, H.H., Bliss, D.B.: The physical mechanism of flow-induced fluctuations in cavities and concepts for their suppression. AIAA-1975-491 2nd Aeroacoustics conference, Hampton, March (1975)
5. Tam, C.-J., Orkwis, P.D., Dissimile, P.J.: On the tones and pressure oscillations induced by flow over rectangular cavities. J. Fluid Mech. **89**, 373–399 (1978)
6. Unalmis, O.H., Clemens, N.T., Dolling, D.S.: Cavity oscillation mechanisms in high-speed flows. AIAA J. **42**, 2035–2041 (2004)
7. Mallinson, S.G., Jackson, A.P., Hillier, R., Kirk, D.C., Soltani, S., Zanchetta, M.: Gun tunnel flow calibration: defining input conditions for hypersonic flow computations. Shock Waves **10**, 313–322 (2000)
8. Jackson, A., Hillier, R., Soltani, S.: Experimental and computational study of laminar cavity flows at hypersonic speeds. J. Fluid Mech. **427**, 329–358 (2001)
9. Hillier, R. et al.: Development of some hypersonic benchmark flows using CFD and experiments. Shock Waves **13**, 375–384 (2003)
10. Creighton, S.: Hypersonic flow over non-rectangular cavities. Thesis, Imperial College London, UK (2003)
11. Creighton, S., Hillier, R.: Experimental and computational study of unsteady hypersonic cavity flows. Aeronaut. J. **111**, 673–688 (2007)
12. Murray, N., Hillier, R.: Axisymmetric separated shock-wave boundary-layer interaction. In: 26th International Symposium on Shock Waves, Goettingen (2007)
13. Menter, F.R.: Eddy viscosity transport equations and their relation to the k-epsilon model. NASA STI/Recon Technical Report no. 95 (1994)
14. Murray, N.: Three-dimensional turbulent shock-wave/boundary-layer interactions in hypersonic. Thesis, Imperial College London, UK (2006)
15. Denison, M.R., Baum, E.: Compressible free shear layer with finite initial thickness. AIAA J. **1**, 342–349 (1963)
16. Kubota, T., Dewey, C.F.: Momentum integral methods for the laminar free shear layer. AIAA J. **2**, 625–629 (1964)
17. Charwat, A., Der, J.: Studies on laminar and turbulent free shear layers with a finite initial boundary layer at separation. AGARD CP No. 4 (1966)
18. Bauer, R.C., Dix, R.E.: Engineering model of unsteady flow in a cavity. Arnold Engineering Development Center, AEDC-TR-17 (1975)
19. Cattafesta, L., Shukla, D., Garg, S., Ross, J.: Development of an adaptive weapons-bay suppression system. In: AIAA-1999-1901 5th Aeroacoustics Conference and Exhibit, Bellevue, May 1999
20. Kegerise, M.A., Spina, E.F., Garg, S., Cattafesta, L.N.: Mode-switching and nonlinear effects in compressible flow over a cavity. Am. Inst. Phys. **16**, 678–687 (2004)
21. Ukeiley, L., Ponton, M., Seiner, J., Jansen, B.: Suppression of pressure loads in cavity flows. AIAA J. **42**, 70–79 (2004)
22. Zhang, X., Edwards, J.A.: An investigation of supersonic oscillatory cavity flows driven by thick shear layers. Aeronaut. J. **94**, 355–364 (1990)